Environmental
Science
Nano

PAPER

View Article Online
View Journal

Published on 30 March 2022. Downloaded by Guangdong Technology University Library on 4/29/2022 3:10:18 AM.

Cite this: DOI: 10.1039/d2en00103a

Near-infrared light induced adsorption–desorption cycle for VOC recovery by integration of metal–organic frameworks with graphene oxide nanosheets†

Hongli Liu,[ab] Ningyun Li,[ab] Mengying Feng,[ab] Guiying Li,[ab] Weiping Zhang[ab] and Taicheng An *[ab]

Received 31st January 2022,
Accepted 29th March 2022

DOI: 10.1039/d2en00103a

rsc.li/es-nano

Metal–organic frameworks are appealing candidates for adsorption of VOCs from contaminated air due to their outstanding capturing capacities, but the traditional regeneration methods of used MOF adsorbents often suffer from great energy-penalty. Herein, a near-infrared light induced desorption of VOCs from a photodynamic GO@MIL-101 nanocomposite adsorbent was attempted by the integration of MIL-101 with GO nanosheets. MIL-101 uniformly and closely grown on GO nanosheets not only rendered inherent excellent VOC adsorption capability, but also enabled it to manifest strong light-harvesting in the whole UV-vis-NIR region. More importantly, GO nanosheets could serve as "nanoheaters" to convert incident light into thermal energy upon exposure to UV-vis or UV-vis-NIR light, and then the localized thermal energy would rapidly transfer and distribute to MIL-101 located on GO nanosheets, thus making GO@MIL-101 nanocomposites reach higher surface temperatures compared to pure MIL-101 and GO counterparts regardless of UV-vis irradiation or UV-vis-NIR irradiation. Eventually, such light induced localized heat would trigger the complete release of adsorbed ethyl acetate from GO@MIL-101 nanocomposites. Distinct from traditional thermal swing desorption, this light induced VOC release could not only mitigate the drawback of MOF of inferior thermal conductivity, but also would provide a potentially low energy strategy for highly efficient regeneration of MOF-based adsorbents powered by naturally abundant solar light without other energy inputs.

Environmental significance

Metal–organic frameworks have been considered as a kind of promising adsorbent for VOC removal, whereas their regeneration often suffers from great energy-penalty due to their inherent inferior thermal conductivity. Herein, a photodynamic adsorbent was constructed by the integration of graphene oxide nanosheets with MIL-101. Upon exposure to UV-vis-NIR light, the GO@MIL-101 nanocomposites would induce localized heat, thus triggering complete desorption of ethyl acetate from GO@MIL-101 and realizing efficient regeneration of the adsorbent. Distinct from traditional thermal desorption, this light induced VOC desorption could not only mitigate the drawback of MOF of inferior thermal conductivity, but also would provide a potentially low energy strategy for highly efficient regeneration of MOF-based adsorbents powered by naturally abundant solar light without other energy inputs.

1. Introduction

Volatile organic compounds (VOCs) emitted from industrial processes are becoming one of the main atmospheric pollutants.[1–3] They not only bring severe environment issues including photochemical smog and secondary organic aerosols, but also threaten human health by inducing diseases such as mutagenesis, headaches, cancer and even death.[4,5] In view of these premises, various techniques for VOC elimination have been exploited, including adsorption, catalytic oxidation, photocatalytic degradation and biofiltration.[2,3,6–9] Among them, considerable research interest has been attracted to the adsorption technique,[2,7] in

---

[a] *Guangdong Key Laboratory of Environmental Catalysis and Health Risk Control, Guangdong-Hong Kong-Macao Joint Laboratory for Contaminants Exposure and Health, Institute of Environmental Health and Pollution control, Guangdong University of Technology, Guangzhou 510006, China. E-mail: antc99@gdut.edu.cn*

[b] *Guangdong Engineering Technology Research Center for Photocatalytic Technology Integration and Equipment, Guangzhou Key Laboratory of Environmental Catalysis and Pollution Control, School of Environmental Science and Engineering, Guangdong University of Technology, Guangzhou 510006, China*

† Electronic supplementary information (ESI) available: XRD data, FT-IR spectra, TEM images, pore-size distribution curves, acidity, as well as additional adsorption and desorption results. See DOI: **https://doi.org/10.1039/d2en00103a**

Published on 30 March 2022. Downloaded by Guangdong Technology University Library on 4/29/2022 3:10:18 AM.

which VOCs could be captured and concentrated by the adsorbent, and subsequently the adsorbed VOCs are expected to be released and recovered. In this regard, apart from high adsorption capacity, release of VOCs from the adsorbent is also critical to improve the working capacity and the economy of the adsorption technique.

Compared with the commonly used porous adsorbents such as zeolites, activated carbon and silica, metal–organic frameworks (MOFs) have been demonstrated to be an optimal choice for the removal of VOCs.[2,10–14] Beyond large specific surface area and high volume, MOFs as an important class of emerging porous materials possess unique characteristics including highly regular pores, ordered structure, abundant interconnected 3D channels and facile functionalization,[14–16] which are beneficial to exploit advanced VOC adsorbents. Accordingly, a large number of MOF-based adsorbents have been attempted for the VOC removal from polluted air and usually afford relatively excellent adsorption capacities compared with conventional porous adsorbents.[2,11–18] Unfortunately, the majority of research mainly focuses on the improvement in adsorption capacities or stability of MOF-based adsorbents, whereas the development of an efficient strategy for VOC desorption from MOF-based adsorbents gained little progress. Like other types of VOC adsorbents, regeneration of MOF-based adsorbents still relies on pressure and/or thermal swing processes, which usually involve high energy penalty;[19] especially for the thermal swing process, MOF-based adsorbents heated by the traditional heating method often suffer from low efficient and non-uniform heating due to the inherent inferior thermal conductivity of MOF, resulting in energy-consuming and slow desorption kinetics.[20,21] Therefore, to improve the practical application potential of MOFs in the removal of VOCs, the development of advanced adsorption systems with highly efficient desorption regenerability while retaining excellent adsorption capability is extremely imperative.

Recently, graphene oxide (GO) nanosheets have displayed the ability to efficiently adsorb broadband light from the UV to near-infrared region (NIR) and convert incident light into thermal energy, which makes GO be applied in various fields such as photochemotherapy, sensors, seawater desalination, biomedicine and photothermal catalysis.[22–27] In these processes, GO could work as a "nanoheater" to generate localized heating and then transfer heat to its surroundings due to its excellent thermal conductivity. Besides, abundant oxygen-containing functional groups existing on the surface of GO nanosheets offer the possibility to coordinate with metal precursors of MOF prior to the MOF synthesis, which could serve as nucleation sites for the growth of MOF on GO nanosheets.[28–30] The resulting GO@MOF composites have demonstrated that they could retain the porosity and morphology of MOF, and might even afford optimized adsorption performance compared to the individual components.[29,30] Consequently, if MOF nanoparticles could uniformly grow on the surface of GO nanosheets, the light induced thermal energy by GO nanosheets would promptly transfer to the whole MOF nanoparticle upon light irradiation due to the excellent thermal conductivity of GO nanosheets and short heat transfer distance, thereby effectively overcoming the poor thermal conductivity of MOF. Distinct from the traditional heating method, this light induced localized heating occurred within the GO nanosheets and nearby MOF nanoparticles, which will be conducive to triggering highly efficient VOC release from GO@MOF without heating the entire adsorbent bed. Moreover, the utilization of naturally abundant solar light at negligible cost to trigger VOC release from the adsorbent offers an economical and sustainable strategy for the regeneration of adsorbents.

Herein, the GO@MIL-101 nanocomposites with different GO contents were synthesized, and their potential as an adsorbent for VOC adsorption and light induced regeneration was also evaluated. The choice of MIL-101 was based on its high surface area, large pore size and excellent structural stability.[31,32] As expected, the obtained GO@MIL-101 nanocomposites could manifest strong light-harvesting properties in the whole UV-vis-NIR region. Upon exposure to light irradiation, the surface temperatures of GO@MIL-101 nanocomposites elevated rapidly by converting the absorbed incident light to heat, and the GO@MIL-101 nanocomposite with 5% GO amount gave the optimal photothermal performance. Driven by such light induced localized heat, the adsorbed ethyl acetate on GO@MIL-101 nanocomposites was promptly released, thereby realizing the efficient regeneration of the GO@MIL-101 adsorbent. Furthermore, a possible mechanism for the light induced desorption of ethyl acetate from the GO@MIL-101 adsorbents was also attempted.

2. Experimental section

2.1 Materials preparation and characterization

All chemical reagents were of analytical grade and used without further purification.

Synthesis of MIL-101. MIL-101 was synthesized under hydrothermal conditions according to the procedure reported in the literature with slight modifications.[31] Firstly, chromium chloride hexahydrate ($CrCl_3·6H_2O$), terephthalic acid and deionized water in a molar ratio of 1 : 1 : 500 were loaded into a stainless-steel autoclave and heated at 190 °C for 16 h. After cooling to room temperature, the slurry was filtered with a G2 glass filter and then isolated with a G4 glass filter. The obtained solid was thoroughly washed with DMF and water. Finally, the as-synthesized sample was treated under vacuum at 150 °C for 12 h.

Synthesis of GO@MIL-101 nanocomposites. Graphite Oxide (GO) was purchased from Nanjing XFNANO Materials Tech Co., Ltd. Initially, the GO aqueous suspension (3 mg mL^{-1}) was prepared by ultrasound for 6 h. Then, $CrCl_3·6H_2O$ was added to a certain volume of the above GO aqueous suspension and was stirred for 1 h. Afterwards, terephthalic acid and deionized water were added into the mixture. After solvothermal reaction at 190 °C for 16 h, the solid was vacuum filtrated, washed and dried in a vacuum under

This journal is © The Royal Society of Chemistry 2022

Published on 30 March 2022. Downloaded by Guangdong Technology University Library on 4/29/2022 3:10:18 AM.

similar procedures to MIL-101. The samples with GO amounts of 2, 5 and 10 wt% were named 2%, 5% and 10% GO@MIL-101, respectively.

The crystal structures of prepared samples were confirmed by powder X-ray diffraction on a Bruker D8 diffractometer equipped with a Cu Kα radiation source. UV-vis-NIR diffuse reflectance spectra were measured on a Shimadzu UV-3600 spectrophotometer and $BaSO_4$ was employed as a reference. Fourier transform-infrared spectra (FT-IR) were collected on a Nicolet iS10 instrument with KBr pellets in the region of 4000–600 cm^{-1}. The porosity and specific surface areas of the samples were studied by N_2 isothermal adsorption–desorption at 77 K using a Micromeritics ASAP 2020. Before measurement, the samples were purified by vacuum degassing at 150 °C for 6 h. The specific surface areas were calculated using the BET and Langmuir equations, respectively. The morphological and structural properties of the samples were observed on a JEM-2010HR transmission electron microscope with an energy dispersive spectrometer. The surface acidities of Lewis acid were obtained based on the chemisorbed-pyridine IR results. The surface temperatures of the samples after exposure to UV-vis light and UV-vis-NIR light were recorded using an infrared camera (Fluke TiX640).

2.2 Adsorption experiments

The adsorption performance of the samples for ethyl acetate was evaluated in a constant flow mode at 30 °C and ambient pressure. Typically, about 0.035 g of adsorbent was loaded into a fixed-bed quartz reactor and further heated at 120 °C for 4 h in N_2 flow to clean the surface of the adsorbent before adsorption experiment. The size of this cuboid quartz reactor is 1.5 cm × 1.0 cm × 0.1 cm to maximize the exposure of the adsorbent to incident light and penetration of incident light into the adsorbent. When the temperature dropped to 30 °C, a 30 mL min^{-1} gas mixture containing 500 ppm ethyl acetate vapor was switched to the reactor to begin the adsorption trial. An online gas chromatograph with two flame ionization detectors was employed to monitor the composition of the outlet gas. The adsorption process was completed until the adsorption equilibrium was reached as indicated by the outlet concentration of ethyl acetate. Subsequently, the desorption experiment was carried out by illuminating the saturated adsorbent and a 30 mL min^{-1} N_2 flow was chosen as the carrier gas. The light source was a 300 W Xe lamp that was vertically placed 10 cm above the reactor. The adsorption capacity and desorption capacity of the adsorbent were determined based on its breakthrough curve and desorption curve, respectively.

The adsorption amount of the adsorbent (q_t) was obtained based on eqn (1):

$$q_t = \frac{V}{1000m}\left(C_0 t - \int_0^t C_t \mathrm{d}t\right) \tag{1}$$

The desorption amount of the adsorbent (q_t) was calculated using eqn (2):

$$q_t = \frac{V}{1000m}\int_0^t C_t \mathrm{d}t \tag{2}$$

where C_0 (mg L^{-1}) refers to the inlet concentration of ethyl acetate, C_t (mg L^{-1}) represents the outlet concentration of ethyl acetate at a given time, V (mL min^{-1}) represents the volumetric flow rate of the inlet gas, m (g) refers to the weight of the adsorbent loaded into the quartz reactor, and t (min) refers to the adsorption or desorption time.

Three kinetic models were used to study the adsorption data and fit the dynamics parameters. The pseudo-first-order, pseudo-second-order and Avrami kinetic model are written as eqn (3)–(5), respectively:

$$q_t = q_e(1 - \exp(-k_f t)) \tag{3}$$

$$q_t = \frac{k_s {q_e}^2}{1 + k_s q_e t} \tag{4}$$

$$q_t = q_e[1 - \exp(-k_a t)^{n_a}] \tag{5}$$

where q_t and q_e (mg g^{-1}) are the ethyl acetate adsorption amount of the adsorbent at a given time t (min) and the equilibrium adsorption amount, respectively, k_f (min^{-1}) represents the first order rate constant, k_s (min^{-1}) represents the second order rate constant, k_a (min^{-1}) represents the Avrami rate constant and n_a is the Avrami exponent which could reflect the possible changes of the adsorption mechanism.

2.3 *In situ* diffuse reflectance Fourier transform infrared spectroscopy (DRIFTS) measurements

Ethyl acetate adsorption and photothermal desorption on the prepared adsorbents were recorded on a Thermo Scientific Nicolet iS10 Fourier transform infrared spectrometer equipped with a MCT detector. Prior to each adsorption test, the adsorbent was loaded into a porous screen at the bottom of a Harrick Scientific Praying Mantis diffuse reflectance cell which had two ZnSe windows and one glass observation window and then the cell was sealed with a dome. Subsequently, the adsorbent was purged at 150 °C in a 30 mL min^{-1} N_2 flow for 2 h. After cooling to 30 °C, a background spectrum of the adsorbent was firstly obtained in the N_2 flow, followed by switching N_2 to ethyl acetate stream (30 mL min^{-1}) for the adsorption experiment. After 80 min of the ethyl acetate adsorption, the ethyl acetate stream was switched to a 30 mL min^{-1} N_2 flow, and meanwhile the Xe lamp was turned on to initiate the desorption process. All DRIFT spectra were recorded at a resolution of 4 cm^{-1} in the range of 4000 to 400 cm^{-1}.

2.4 Temperature programmed desorption experiments

The desorption activation energies of ethyl acetate adsorbed onto MIL-101 and GO@MIL-101 nanocomposites were calculated by temperature programmed desorption (TPD) experiments. Typically, 0.03 g of adsorbent was placed into a

Published on 30 March 2022. Downloaded by Guangdong Technology University Library on 4/29/2022 3:10:18 AM.

quartz reactor cell and pretreated in 30 mL min^{-1} He flow at 150 °C for 1 h. After cooling to 30 °C, the adsorbent was exposed to 500 ppm of ethyl acetate steam for 1 h, and then purged with He for 1 h to remove physisorbed ethyl acetate. Subsequently, the TPD spectra were continuously collected with an automatic chemical adsorption instrument (PCA-1200, Beijing Builder Electronic Technology Co., Ltd) in the 300–420 K temperature region at different heating rates in the range of 3 to 7 K min^{-1} under a He flow (30 mL min^{-1}). The desorption activation energies of ethyl acetate onto the MIL-101 and GO@MIL-101 nanocomposites could be estimated by the following eqn (6):

$$-\ln\left(\frac{\beta_{\mathrm{H}}}{RT_{\mathrm{P}}{}^{2}}\right)=\frac{E_{\mathrm{d}}}{RT_{\mathrm{P}}}+\ln\left(\frac{E_{\mathrm{d}}}{k_{0}}\right) \qquad (6)$$

where E_{d} (kJ mol^{-1}) refers to the desorption activation energy of ethyl acetate on the adsorbent, T_{p} (K) represents the peak temperature of the TPD curve, and β_{H} (K min^{-1}) is the heating rate.

3. Results and discussion

3.1 Material characterization

Fig. 1 depicts the X-ray diffraction patterns of MIL-101 and GO@MIL-101 nanocomposites. The characteristic diffraction peaks of the GO@MIL-101 nanocomposites with different GO amounts all were in line with that of pure MIL-101, revealing that the addition of GO nanosheets did not break the structure of MIL-101. Additionally, pure GO nanosheets showed two broad peaks at 2θ of 14.0° and 20.1° (Fig. S1†), which were corresponding to (001) and (002) reflections of graphene.[33,34] Compared with pure GO nanosheets, the prominent diffraction peak of GO at 20.8° appeared in the GO@MIL-101 nanocomposites. Moreover, the intensity of this diffraction peak enhanced with the increase of GO amount. These observations indicated that the GO@MIL-101 nanocomposites were successfully synthesized and preserved the features of both GO nanosheets and MIL-101.

To further verify the structure, FT-IR spectra of MIL-101 and GO@MIL-101 nanocomposites were measured. As displayed in Fig. S2,† the characteristic peaks of GO nanosheets at 1741 and 1637 cm^{-1} belonged to the stretching vibrations of the C=O bond of carbonyl or carboxyl groups. For pure MIL-101, two strong peaks at 1639 and 1423 cm^{-1} correspond to the asymmetric stretching vibration and symmetric stretching vibration of the carboxyl group, respectively.[32,35] As expected, it was observed that all GO@MIL-101 nanocomposites have a similar spectrum to the MIL-101. Nevertheless, two peaks assigned to the C=O bond of GO nanosheets couldn't be observed in the FT-IR spectra of GO@MIL-101 nanocomposites, which would result from the formation of a coordination bond between the GO layers and Cr site of MIL-101.[36]

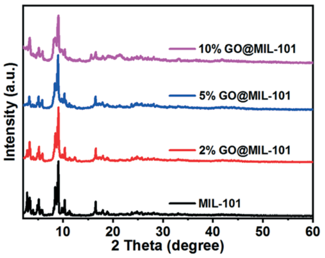

Fig. 1 Powder XRD patterns of pure MIL-101 and GO@MIL-101 nanocomposites with GO loading amounts of 2, 5 and 10 wt%, respectively.

The morphologies of the samples observed by TEM indicated that GO nanosheets possessed a layered structure and stacked together with several wrinkles at the edge of the GO plane (Fig. S3a†). The pure MIL-101 has a regular octahedral shape with the size in the range of 300–500 nm (Fig. S3b†). For the 2% GO@MIL-101 nanocomposite, a few of MIL-101 were partially located on the GO layers and formed aggregative nanocomposites (Fig. 2a). As the GO loading amount was increased, the layered GO could be observed more clearly and MIL-101 nanoparticles were dispersed onto the GO plane more uniformly (Fig. 2). Nevertheless, the size and the shape of MIL-101 particles onto the GO plane were gradually reduced and became a bit irregular with the increased GO loading amount, which were also observed in previous reports.[29,37] These observations were probably attributed to the sufficient interaction between the Cr^{3+} precursor of MIL-101 and the oxygen functional groups in the surface of GO nanosheets as evidenced by FT-IR. This interaction was able to offer abundant nucleation sites for the further assembly of MIL-101 onto GO nanosheets, thus facilitating the dispersion of MIL-101 on GO nanosheets. Meanwhile, it would in turn restrict the growth of MIL-101, leading to reduced dimension and irregular crystal shape of MIL-101 in the GO@MIL-101 nanocomposites. HAADF-STEM imaging and corresponding EDX elemental mapping of the 5% GO@MIL-101 nanocomposite further manifested the uniform distribution of MIL-101 onto the GO surface.

The pore structures and surface areas of the samples were measured by N_2 adsorption–desorption at 77 K and the

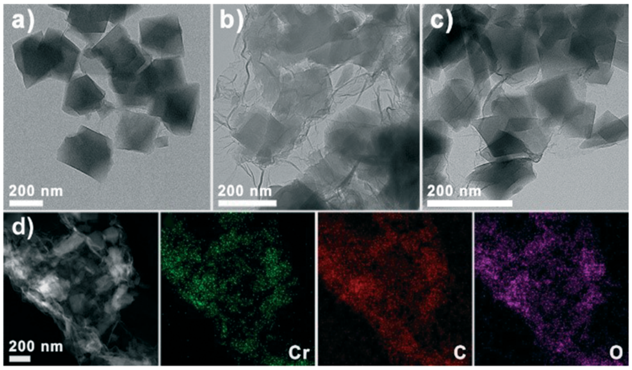

Fig. 2 TEM images of GO@MIL-101 nanocomposites with GO loading amounts of 2 wt% (a), 5 wt% (b) and 10 wt% (c), and the corresponding EDX elemental mapping (d).

This journal is © The Royal Society of Chemistry 2022

Published on 30 March 2022. Downloaded by Guangdong Technology University Library on 4/29/2022 3:10:18 AM.

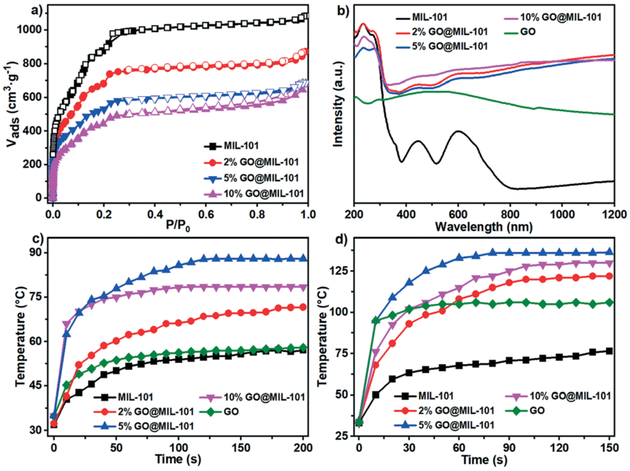

Fig. 3 N_2 adsorption–desorption isotherms (a), ultraviolet-visible-infrared light irradiation diffuse reflectance spectra (b), time-dependent temperature curves under ultraviolet-visible light irradiation (c), and ultraviolet-visible-infrared light irradiation (d) of pure MIL-101, GO and GO@MIL-101 nanocomposites with GO loading amounts of 2, 5 and 10 wt%, respectively.

results are presented in Fig. 3a and S4.† It can be seen that the N_2 adsorption isotherms of pure MIL-101 and GO@MIL-101 nanocomposites with different GO loading amounts all exhibited type-I profiles with secondary uptakes at $P/P_0 \approx 0.1$ and 0.2, demonstrating the presence of micropores and mesopores. Moreover, the pore size distribution curves of GO@MIL-101 nanocomposites were also similar and consistent with that of pure MIL-101 (Fig. S4†). However, the calculated Brunauer–Emmett–Teller (BET) surface area and pore volume of GO@MIL-101 nanocomposites were decreased with the increased GO amount. For pure MIL-101, the BET surface area and pore volume were 3304 $m^2\ g^{-1}$ and 1.67 $cm^3\ g^{-1}$, respectively (Table 1). Comparatively, the GO@MIL-101 nanocomposites with the GO amount of 2, 5 and 10 wt% had the BET surface area of 2586, 1973 and 1721 $m^2\ g^{-1}$, and pore volume of 1.35, 1.06 and 1.19 $cm^3\ g^{-1}$. As observed by TEM in Fig. 2, the GO nanosheets adhered well to the surface of MIL-101 nanoparticles in the GO@MIL-101 nanocomposites, possibly obstructing a part of apertures of MIL-101. On the other hand, the distortion of the MIL-101 structure resulting from the interaction between MIL-101 and GO nanosheets would be responsible for another reason for their declined BET surface area and pore volume.

To obtain the optical properties of GO, MIL-101 and GO@MIL-101 nanocomposites, the UV-vis-NIR diffuse reflection spectra were collected in the region of 200–1200 nm. As depicted in Fig. 3b, a strong absorption peak of pure MIL-101 at 235 nm would derive from the π–π* transitions of ligands, and two absorption peaks at *ca.* 440 and 600 nm might result from the d–d spin transition of the Cr^{3+}.[38,39] As a blackbody material, GO exhibited a strong light-harvesting property in all the investigated regions. Remarkably, the three GO@MIL-101 nanocomposites not only preserved the characteristic absorption peaks of both MIL-101 and GO nanosheets, but also displayed higher light-harvesting intensities compared with pure MIL-101 and GO nanosheets, especially in the visible and near-infrared regions. The enhanced light-harvesting properties of GO@MIL-101 nanocomposites would be attributed to the strong interaction between GO and MIL-101, which has been proved by the FT-IR results. The above observations demonstrated that the optical properties of MIL-101 can be effectively improved by reasonable integration of MIL-101 and GO nanosheets. Importantly, the outstanding light harvesting properties may endow GO@MIL-101 nanocomposites with great potential toward photothermal conversion.

Table 1 Characterization results of MIL-101 and GO@MIL-101 nanocomposites

Sample	S_{BET} ($m^2\ g^{-1}$)	$S_{Langmuir}$ ($m^2\ g^{-1}$)	V_{pore} ($cm^3\ g^{-1}$)
MIL-101	3304	4678	1.67
2% GO@MIL-101	2586	3604	1.35
5% GO@MIL-101	1973	2854	1.06
10% GO@MIL-101	1721	2563	1.19

In order to further investigate the photothermal properties, the GO@MIL-101 nanocomposites, GO nanosheets, and MIL-101 samples were exposed to UV-vis light and UV-vis-NIR light, respectively, while their surface temperatures were measured with a thermal imaging infrared camera. As shown in Fig. 3c, the surface temperatures of pure GO nanosheets and MIL-101 increased and stayed around 57 °C after 150 seconds of UV-vis light illumination, and the GO nanosheets exhibited a slightly faster temperature elevation than MIL-101. In contrast, the surface temperatures of the GO@MIL-101 nanocomposites with 2, 5 and 10 wt% GO amounts were quickly elevated to 74.7, 88.0 and 78.5 °C within 140 seconds of UV-vis light illumination. Considering the excellent light-harvesting properties of GO@MIL-101 nanocomposites and GO nanosheets in the whole UV-vis-NIR light region, we further investigated their photothermal properties under UV-vis-NIR light illumination. Interestingly, the surface temperature of GO nanosheets was rapidly boosted to 100 °C within 30 seconds of UV-vis-NIR light illumination, whereas the surface temperature of MIL-101 gently reached 70.8 °C within 90 seconds of UV-vis-NIR light illumination (Fig. 3d), demonstrating that GO was more efficient than MIL-101 for the conversion of UV-vis-NIR light to thermal energy. As expected, the three GO@MIL-101 nanocomposites all presented higher stable temperatures compared with pure GO and MIL-101. Moreover, the 5% GO@MIL-101 nanocomposite displayed optimal surface temperature which quickly increased to over 130 °C within 50 seconds of UV-vis-NIR light illumination. It should be noted that the surface temperatures of the three GO@MIL-101 nanocomposites were much higher than that of pure GO and MIL-101 whether under UV-vis light illumination or UV-vis-NIR light illumination, implying that the integration of GO nanosheets and MIL-101 was capable of improving the light-to-thermal conversion properties.

Published on 30 March 2022. Downloaded by Guangdong Technology University Library on 4/29/2022 3:10:18 AM.

3.2 Dynamic adsorption of ethyl acetate onto the adsorbent

The dynamic adsorption behaviors of 500 ppm ethyl acetate onto MIL-101 and GO@MIL-101 nanocomposites were evaluated under a gas flow rate of 30 mL min^{-1} at 303 K. As depicted in Fig. 4a, it can be seen that the breakthrough curves of MIL-101 and GO@MIL-101 nanocomposites presented similar shapes. At the beginning of the adsorption test, the ethyl acetate outlet concentration instantly declined to near zero within 5 min and then maintained for some time. Once the breakthrough occurred, the ethyl acetate outlet concentration gradually elevated and subsequently reached adsorption equilibrium. However, the breakthrough time and equilibrium time of MIL-101 were a bit longer than those of the GO@MIL-101 nanocomposite. As for pure MIL-101, the equilibrium adsorption time for ethyl acetate adsorption was 370 min. In contrast to MIL-101, the GO@MIL-101 adsorbents with 2, 5 and 10 wt% GO amounts showed shorter equilibrium adsorption times of 310, 320 and 190 min, respectively. Based on the breakthrough curves, the estimated equilibrium adsorption capacities of MIL-101 and the GO@MIL-101 adsorbents with 2, 5 and 10 wt% GO amounts according to eqn (1) were 389.5, 299.9, 275.5 and 242.3 mg g^{-1} (Table S1†), respectively. Noticeably, the equilibrium adsorption capacities of the adsorbents were obviously in line with the order of their specific surface areas and total pore volumes (Fig. 3a). Considering the similar pore size of the four adsorbents, it is reasonable to infer that the specific surface area and total pore volume would play an important role in ethyl acetate adsorption.

To analyze the adsorption kinetics of ethyl acetate onto the MIL-101 and GO@MIL-101 adsorbents, three kinetic models including pseudo-first-order, pseudo-second-order and Avrami kinetic models were applied to fit the ethyl acetate uptake curves, respectively. Firstly, the evolution of the amounts of ethyl acetate adsorbed onto the four adsorbents with time (Fig. 4b and c, S5 and S6†) was estimated from their corresponding breakthrough curves based on eqn (1). The values of the kinetic parameters obtained by the three different models and their corresponding correlation coefficients of R^2 are presented in Table 2. Obviously, the kinetic constant (k_f, k_s and k_a) of the three GO@MIL-101 adsorbents was higher than that of pure MIL-101 with any kinetic model employed, revealing the enhancement of adsorption kinetics after the integration of MIL-101 with GO nanosheets. As can be seen in Fig. 4b and c and S5 and S6,† the pseudo-first-order and pseudo-second-order kinetic models both overestimated ethyl acetate adsorption onto the MIL-101 and GO@MIL-101 adsorbents in the initial stages and the final stages. The Avrami kinetic model exhibited the best fitting quality among the three kinetic models for predicting ethyl acetate onto the four adsorbents. Furthermore, the correlation coefficients (R^2) of the pseudo-first-order, pseudo-second-order and Avrami kinetic models summarized in Table 2 fell within the range of 0.985–0.994, 0.983–0.999 and 0.988–0.996, respectively. By comparison of the adsorption amounts between their predicted and experimental values, the predicted adsorption amounts by the Avrami kinetic model were most close to their experimental values, and the pseudo-second-order kinetic model provided the worst fitted values. The above results indicated that the Avrami kinetic model would be most adequate for describing the ethyl acetate adsorption behaviors onto the MIL-101 and GO@MIL-101 adsorbents.

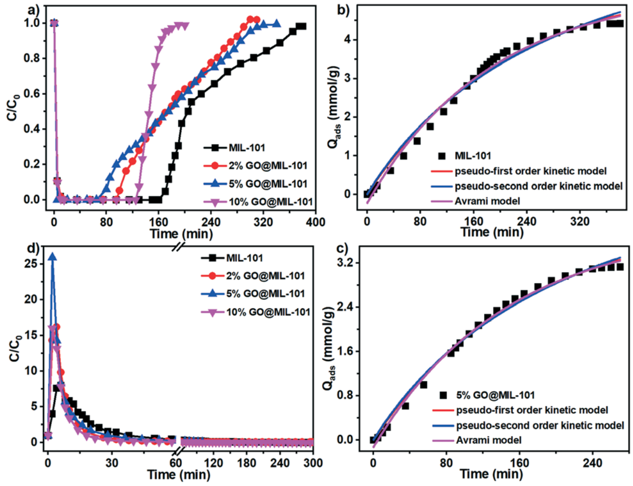

Fig. 4 The breakthrough curves (a) of ethyl acetate onto pure MIL-101 and GO@MIL-101 adsorbents, experimental ethyl acetate uptake (symbols) and corresponding fitting curves (lines) by pseudo-first-order, pseudo-second-order and Avrami kinetic models of pure MIL-101 (b) and 5% GO@MIL-101 nanocomposite (c), and their corresponding desorption curves under irradiation with a 300 W Xe lamp (d).

It is well accepted that the pseudo-first-order model is usually used to describe reversible adsorption based on physical interactions, and the pseudo-second-order kinetic model is proposed for the assumption of the strong interaction between the adsorbate and adsorbent.[40,41] The Avrami kinetic model has been widely adopted to explain a hybrid chemical and physical adsorption mechanism.[41–44] Given the excellent fit of the Avrami kinetic model, it could be concluded that a strict physical or chemical adsorption mechanism seemed to be incapable of describing the adsorption behaviors, and a hybrid chemical and physical adsorption should be involved in the adsorption of ethyl acetate onto the MIL-101 and GO@MIL-101 adsorbents. Moreover, the Avrami exponent (n_a) is always used to reflect heterogeneous adsorption sites and possible mechanism variations during the adsorption process.[41,42] As observed in Table 2, the n_a values obtained from the MIL-101 and GO@MIL-101 adsorbents varied little, suggesting that the adsorption mechanism among the four adsorbents did not change.

3.3 *In situ* photothermal desorption and recycling performance

To evaluate the photothermal desorption properties of the adsorbents, the *in situ* desorption experiments were firstly carried out using a Xe lamp with a wavelength range of 200–780 nm as a light source after their absorption equilibriums were achieved (Fig. 4). As displayed in Fig. 4d, the ethyl

Published on 30 March 2022. Downloaded by Guangdong Technology University Library on 4/29/2022 3:10:18 AM.

Table 2 Coefficients of adsorption kinetic equations of ethyl acetate onto various adsorbents with different adsorption models

	Pseudo-first-order			Pseudo-second-order			Avrami model			
Sample	q_e (mg g^{-1})	k_f (10^{-3} min^{-1})	R^2	q_e (mg g^{-1})	k_s (min^{-1})	R^2	q_e (mg g^{-1})	k_a (10^{-3} min^{-1})	n_a	R^2
MIL-101	490.8	4.74	0.988	748.1	0.39	0.984	470.5	5.37	1.04	0.991
2% GO@MIL-101	376.2	5.81	0.993	566.6	0.64	0.999	362.1	6.52	1.04	0.995
5% GO@MIL-101	355.1	6.14	0.994	543.6	0.69	0.992	341.0	6.87	1.03	0.996
10% GO@MIL-101	392.1	5.62	0.985	662.6	0.45	0.983	356.9	6.84	1.04	0.988

acetate concentration in the outlet was promptly elevated within 5 min of irradiation and then declined for all the MIL-101 and GO@MIL-101 adsorbents, which was also observed in our previous reports.[8,45] This phenomenon would be highly associated with their excellent adsorption capacities. It is obvious that the desorption kinetics of GO@MIL-101 adsorbents was favored as the GO amount increased and the 5% GO@MIL-101 nanocomposite exhibited the fastest desorption process. Impressively, the C/C_0 of the 5% GO@MIL-101 nanocomposite reached 25.9 within 2 min of irradiation, while the highest C/C_0 was obtained to be merely 8.0 for MIL-101 within 6 min of irradiation. More importantly, complete desorption of the adsorbed ethyl acetate onto the 5% GO@MIL-101 adsorbent could be achieved within 98 min of irradiation. But it was difficult to reach complete desorption of the adsorbed ethyl acetate onto MIL-101 despite 300 min irradiation with the corresponding desorption efficiency of 74.4% (Table S1†). Noticeably, approximately 77.8%, 96.5% and 80.0% of the adsorbed ethyl acetate onto the GO@MIL-101 nanocomposites with 2, 5 and 10 wt% GO amounts could be recovered within 60 min of irradiation, showing a promising improvement in the ethyl acetate desorption. But their desorption efficiency became very slow under the subsequent irradiation. The introduction of GO nanosheets to MIL-101 could raise the surface temperature due to their excellent photothermal effects (Fig. 3c), which is conducive to the ethyl acetate desorption. On the other hand, strong interactions between the adsorbate and adsorbent often require a higher desorption temperature. Considering the existence of a hybrid chemical and physical adsorption in the ethyl acetate adsorption process as inferred by the results of adsorption kinetics, it was understandable that the adsorbed ethyl acetate by physical interaction would be released quickly and some adsorbed ethyl acetate by chemical interaction would be desorbed difficultly, thereby denoting a fast desorption in the initial irradiation and a very sluggish desorption in the later irradiation.

Reusability of the adsorbent is of great significance in the adsorption process which is an essential parameter to evaluate its practical application potential. Therefore, five adsorption–desorption cycle tests were performed with the optimal 5% GO@MIL-101 adsorbent. As observed in Fig. 5a, the shapes of the adsorption curves of the 5% GO@MIL-101 nanocomposite were similar and their adsorption capacities were essentially no loss with an average adsorption capacity of 271.0 ± 4.6 mg g^{-1} during the five adsorption–desorption runs (Table S2†). Moreover, the desorption behaviors of ethyl acetate onto the 5% GO@MIL-101 nanocomposite also remained unchanged and little change of desorption efficiency was observed during the five adsorption–desorption cycle tests (Fig. 5b). These results demonstrated that the regeneration of the GO@MIL-101 nanocomposite was readily achieved even under the UV-vis light irradiation. For the comparison, the reusability of pure MIL-101 was also investigated under the same conditions. Given that the ethyl acetate desorption onto pure MIL-101 was considerably tardy, each desorption time was fixed at 300 min. Obviously, the adsorption capacity and desorption capacity declined by 19.3% and 11.5% in the second run (Fig. 5c and d and Table S3†), respectively. However, little change in the adsorption capacity and desorption capacity was observed from the second to the fifth runs, which might be relevant to the different kinds of adsorption sites onto pure MIL-101 and its lower surface temperature under light irradiation. That is, a portion of ethyl acetate adsorbed onto MIL-101 by strong interactions was difficult to release and would remain, leading to reduced adsorption capacity. The above results revealed that the introduction of GO nanosheets to MIL-101 was an effective strategy to boost the ethyl acetate desorption, thus enabling GO@MIL-101 nanocomposites to be an outstanding adsorbent with high adsorption properties and excellent reusability under light irradiation. Furthermore, the characteristic diffraction peaks of both the MIL-101 and 5%

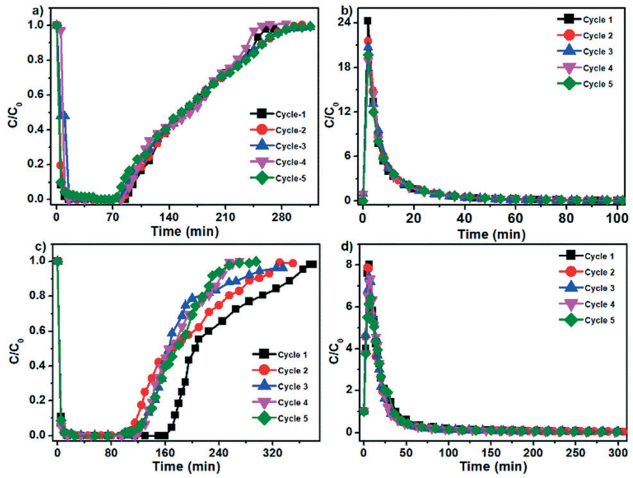

Fig. 5 The ethyl acetate adsorption–desorption cycle performance of the 5% GO@MIL-101 nanocomposite (a and b) and pure MIL-101 (c and d) under ultraviolet-visible light irradiation.

Published on 30 March 2022. Downloaded by Guangdong Technology University Library on 4/29/2022 3:10:18 AM.

GO@MIL-101 after five adsorption–desorption cycles showed no appreciable changes as compared to their fresh counterparts (Fig. S7† and 1), implying excellent structural stability of MIL-101 and GO@MIL-101 under the investigated adsorption and desorption conditions.

To better understand the photothermal desorption process, *in situ* desorption experiments were further performed using a Xe lamp with a wavelength range of 200–1200 nm as the light source. Initially, the adsorption equilibrium of MIL-101 and 5% GO@MIL-101 nanocomposite was accomplished (Fig. 6a) and then the adsorbents were exposed to UV-vis-NIR light. The desorption efficiencies of MIL-101 and 5% GO@MIL-101 nanocomposite were distinctly higher than their corresponding results under the UV-vis light irradiation (Fig. 6b and 4d). Moreover, the ethyl acetate adsorbed onto the 5% GO@MIL-101 nanocomposite could be completely released within 60 min of irradiation (Table S4†). The above results further suggested that the photothermal performance was a dominant factor for the desorption of ethyl acetate onto investigated adsorbents. In addition, the ethyl acetate desorption performance over 5% GO@MIL-101 was investigated at 90 °C by the traditional heating method (Fig. S8†). In every case, the desorption time needed to obtain equal desorption amount was longer for the traditional heating method. Considering the excellent photothermal property of GO, a local temperature gradient could appear at the interface between GO and MIL-101, which would be associated with the faster ethyl acetate desorption rate over 5% GO@MIL-101 by UV-vis light irradiation than traditional heating.

3.4 Regeneration mechanism of the adsorbents

To grasp intuitively the possible interactions between ethyl acetate and the adsorbent, *in situ* DRIFT experiments were also carried out to monitor the adsorption and photothermal desorption of ethyl acetate onto MIL-101 and GO@MIL-101 nanocomposites. Before the ethyl acetate adsorption, MIL-101 and 5% GO@MIL-101 nanocomposite afforded similar main vibrational bands, yet both the intensities and locations of their characteristic bands were different (Fig. 7a and b), indicating the existence of strong interactions between GO and MIL-101 in the GO@MIL-101 adsorbents. For MIL-101, the bands at 1702, 1648, 1596 and 1560 cm^{-1} were attributed to the typical stretching vibration of the COO$^-$ groups, while the bands at 1513 and 1450 cm^{-1} were assigned to aromatic C═C stretching vibration within the MIL-101 framework.[32,35] After ethyl acetate adsorption onto the 5% GO@MIL-101 nanocomposite, the COO$^-$ asymmetric stretching vibration at 1638 cm^{-1} and the COO$^-$ symmetric stretching vibration at 1567 cm^{-1} were gradually red shifted to 1634 cm^{-1} and 1569 cm^{-1}, respectively, while two bands at 1598 and 1696 cm^{-1} gradually became weak and then totally disappeared. Meanwhile, a new band at 1729 cm^{-1} belonging to the C═O stretching vibration of ethyl acetate emerged, and its intensity was raised as the adsorption time was prolonged. Nevertheless, the bands correlated to aromatic C═C stretching vibration of MIL-101 at 1511 and 1440 cm^{-1} showed no appreciable change. These phenomena were probably caused by strong adsorption of ethyl acetate onto the GO@MIL-101 nanocomposite.[46,47] Given the surface Lewis acidity of the GO@MIL-101 nanocomposite, it was believed that some ethyl acetate would adsorb onto the coordinatively unsaturated Cr site of MIL-101 *via* its C═O bond except for the physical pore filling effect, leading to clear changes in the intensity and position of the COO$^-$ stretching vibration within the GO@MIL-101 nanocomposite.

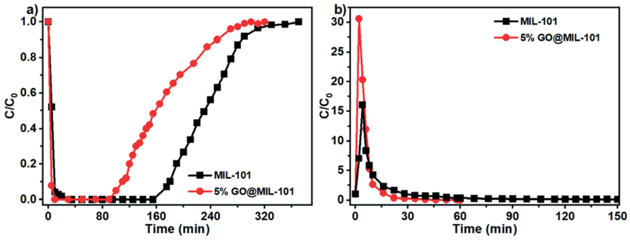

Fig. 6 The ethyl acetate adsorption (a) and desorption performance (b) of the pure MIL-101 and 5% GO@MIL-101 nanocomposite under UV-vis-NIR light irradiation.

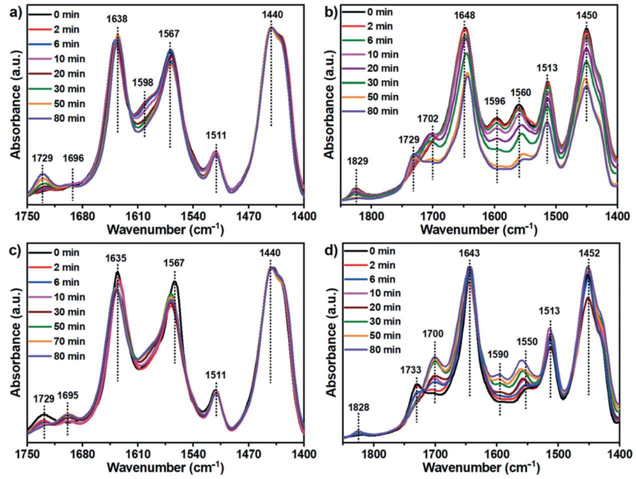

Fig. 7 *In situ* DRIFTS spectra of ethyl acetate adsorbed onto the 5% GO@MIL-101 nanocomposite (a) and pure MIL-101 (b), as well as the corresponding DRIFTS spectra of ethyl acetate desorbed from the 5% GO@MIL-101 nanocomposite (c) and MIL-101 (d).

After the ethyl acetate adsorption onto the 5% GO@MIL-101 nanocomposite within 80 min, the desorption process was initiated by turning on the Xe lamp and followed monitoring by *in situ* DRIFT (Fig. 7c). Distinctly, the intensity of the band at 1729 cm^{-1} for the C═O stretching vibration of ethyl acetate gradually declined and eventually disappeared completely, implying the release of ethyl acetate from the surface of the 5% GO@MIL-101 nanocomposite. The bands at 1635 and 1567 cm^{-1} for the COO$^-$ stretching vibrations of the 5% GO@MIL-101 nanocomposite adsorbed with ethyl acetate presented slight blue shifts of 2 and 4 cm^{-1} with 80 min of irradiation, respectively. At the same time, the band at 1695 cm^{-1} related to the COO$^-$ stretching vibrations of the

Published on 30 March 2022. Downloaded by Guangdong Technology University Library on 4/29/2022 3:10:18 AM.

5% GO@MIL-101 nanocomposite was observed and gradually became strong with extending irradiation time. Significantly, the change trends of the band positions and intensities for both ethyl acetate and GO@MIL-101 nanocomposite during the desorption process were contrary to that in the adsorption process, possibly due to the reversible ethyl acetate adsorption/desorption onto the GO@MIL-101 nanocomposite under irradiation.

For the comparison, the adsorption and photothermal desorption of ethyl acetate onto pure MIL-101 was also measured by *in situ* DRIFT (Fig. 7b and d). Similarly, the vibrations of the characteristic bands of ethyl acetate and MIL-101 were almost in line with that of the 5% GO@MIL-101 nanocomposite regardless of the adsorption and desorption process, demonstrating that the introduction of GO to MIL-101 would not alter the ethyl acetate adsorption behaviors. Nevertheless, more apparent red shifts of the COO^- characteristic bands of MIL-101 during the ethyl acetate adsorption were observed as compared with the 5% GO@MIL-101 nanocomposite. For instance, the COO^- stretching vibrations of MIL-101 at 1648 and 1560 cm^{-1} have remarkable red shifts of 5 and 8 cm^{-1}, whereas the corresponding red shifts onto 5% GO@MIL-101 were only 2 and 4 cm^{-1}, respectively. Additionally, the amounts of Lewis acidic sites onto the 5% GO@MIL-101 nanocomposite were a bit lower than that of pure MIL-101 (Fig. 8a and Table S5†), probably rendering less ethyl acetate chemical adsorption onto GO@MIL-101 nanocomposites *via* the Lewis acid–base interactions between the C═O bond of ethyl acetate and the unsaturated Cr site. This would also be responsible for the more obvious variations in DRIFT spectra during the ethyl acetate adsorption onto pure MIL-101 as compared with the 5% GO@MIL-101 nanocomposite.

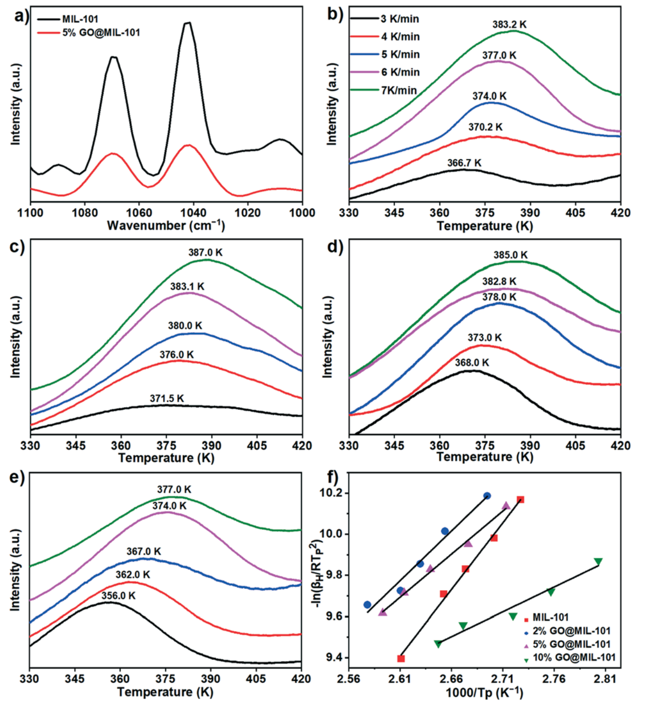

Fig. 8 FT-IR spectra of pyridine adsorbed onto pure MIL-101 and 5% GO@MIL-101 nanocomposite (a), TPD spectra of ethyl acetate adsorption onto the pure MIL-101 (b), GO@MIL-101 nanocomposites with GO loading amounts of 2 (c), 5 (d) and 10 wt% (e), respectively, at different heating rates, as well as the corresponding linear dependence between $\ln[\beta_H/RT_p^2)]$ and $1/T_p$ for TPD of ethyl acetate onto MIL-101 and GO@MIL-101 nanocomposites (f).

Furthermore, the TPD curve of ethyl acetate from 5% GO@MIL-101 at a heating rate of 3 K min^{-1} displayed two separated peaks (Fig. S9†), indicating two major sites in the 5% GO@MIL-101 for ethyl acetate adsorption. Generally, the peak at the lower temperature was the weaker adsorption and the peak at the higher temperature belonged to the stronger adsorption. Based on the results of adsorption kinetics fitting and *in situ* DRIFT experiments, the weaker adsorption would come from physical interactions between the pores in GO@MIL-101 and ethyl acetate, and the slightly stronger adsorption would result from the Lewis acid–base interactions between ethyl acetate and the unsaturated Cr^{3+} metal centers in MIL-101.

To obtain the desorption activation energies of ethyl acetate onto the MIL-101 and GO@MIL-101 adsorbents, a series of TPD tests were also conducted at different heating rates from 3 to 7 K min^{-1}. As presented in Fig. 8b–e, there was an obvious peak in each TPD curve due to the ethyl acetate desorption from the MIL-101 adsorbent. Moreover, the peak temperature (T_p) was elevated with the increase of heating rate (β_H). The straight slope was obtained by plotting $\ln(T_p^2/\beta_H)$ *versus* $1/T_p$ (Fig. 8f). Furthermore, the desorption activation energy of ethyl acetate onto pure MIL-101 was estimated to be 53.9 kJ mol^{-1} based on eqn (6) (Table S6†). In the same way, the desorption activation energies of ethyl acetate onto GO@MIL-101 nanocomposites with GO amounts of 2, 5 and 10 wt% were estimated to be 40.15, 34.82, and 25.69 kJ mol^{-1}, respectively. Evidently, the desorption activation energies of ethyl acetate onto GO@MIL-101 adsorbents were lower than that onto pure MIL-101 and were gradually declined with the increasing GO amounts. These results suggested that the introduction of GO nanosheets to MIL-101 was beneficial to the ethyl acetate desorption.

In view of the above results, a possible mechanism for the enhancement in the photothermal desorption of ethyl acetate from GO@MIL-101 nanocomposites was speculated as follows (Scheme 1). Based on the adsorption properties and

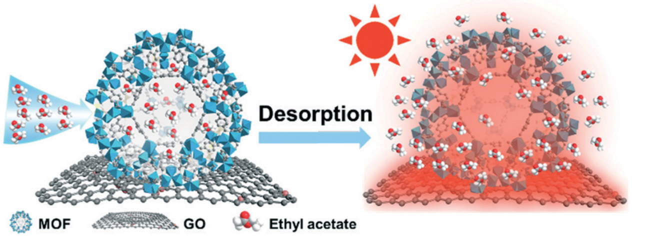

Scheme 1 Illustration of the possible photothermal desorption mechanism of ethyl acetate onto the GO@MIL-101 adsorbent.

Published on 30 March 2022. Downloaded by Guangdong Technology University Library on 4/29/2022 3:10:18 AM.

in situ DRIFT results, it can be obtained that the adsorption mechanism for the ethyl acetate onto GO@MIL-101 nanocomposites was consistent with that onto pure MIL-101. Moreover, the physical pore filling effect was believed as a dominant driving force and chemical interactions were also involved during these adsorption processes. Thus, it is speculated that the differences in the ethyl acetate adsorption properties among the pure MIL-101 and GO@MIL-101 nanocomposites would not play a crucial role in influencing their photothermal desorption properties. As demonstrated by UV-vis diffuse reflectance spectra and an infrared camera, the GO@MIL-101 nanocomposites showed excellent light-harvesting properties in the whole UV-vis-NIR light region and were capable of converting the absorbed light into thermal energy. However, the surface temperatures of pure GO and MIL-101 were distinctly lower than that of GO@MIL-101 nanocomposites. It is well known that GO could show excellent light-harvesting properties in the whole UV-vis-NIR light region, while it is also an excellent photothermal material with high heat-transfer rate.[24,48] Accordingly, it was plausible that the cooperative effect between GO nanosheets and MIL-101 would be responsible for the enhanced surface temperature of the GO@MIL-101 nanocomposite under light irradiation. When the GO@MIL-101 adsorbent was exposed to UV-vis or UV-vis-NIR light, the thermal energy converted by GO nanosheets would transfer instantly to MIL-101 *via* the coordination bonds between GO and MIL-101. Due to the short heat transfer distances inside each MIL-101 nanoparticle, this thermal energy would subsequently distribute over the whole MIL-101 surface by its ordered ligands and metal ions, which could effectively mitigate the intrinsic thermal conductivity shortcoming of MIL-101. Meanwhile, the poor thermal conductivity of the MOF made it minimize additional thermal loss to the ambient environment, thus achieving higher surface temperatures of the GO@MIL-101 nanocomposite than pure MIL-101 and GO regardless of UV-vis light irradiation or UV-vis-NIR light irradiation. Finally, the light induced thermal energy by the GO@MIL-101 adsorbents were high enough to trigger the desorption of adsorbed ethyl acetate, resulting in outstanding reusable and recyclable potential.

4. Conclusion

In summary, an excellent photo-responsive adsorbent was demonstrated by integration of GO nanosheets with MIL-101 for the adsorption and photothermal desorption of ethyl acetate. The obtained GO@MIL-101 nanocomposites reserved the morphology and porosity of both MIL-101 and GO nanosheets, in which several isolated MIL-101 nanoparticles were evenly and closely distributed onto GO nanosheets, thereby affording high adsorption capacity and adsorption kinetics. More importantly, the GO@MIL-101 nanocomposites have the ability to improve the light-to-thermal conversion properties regardless of UV-vis or UV-vis-NIR irradiation due to the excellent cooperative effect between GO and MIL-101, resulting in the enhancement in the surface temperature; especially, the surface temperature of the 5% GO@MIL-101 nanocomposite could be quickly elevated to 88 °C within 140 seconds of exposure to UV-vis light and 130 °C within 50 seconds of exposure to UV-vis-NIR light. Consequently, the adsorbed ethyl acetate onto the GO@MIL-101 nanocomposite could readily realize the complete release whether under UV-vis or UV-vis-NIR irradiation. Moreover, after five adsorption–desorption cycles, no appreciable variation was observed in both the ethyl acetate adsorption and desorption properties onto the 5% GO@MIL-101 nanocomposite even under UV-vis light irradiation. The outstanding adsorption and recycling properties of this potential adsorbent as well as naturally abundant solar light make the adsorption system be low-energy yet highly efficient. It is foreseen that more photothermal adsorbents with better performance will be exploited in further research inspired by this work to enhance the possibility for their practical application.

Conflicts of interest

There are no conflicts to declare.

Acknowledgements

This work was supported by the National Natural Science Foundation of China (41991314, 22076028 and 41731279), Local Innovative and Research Teams Project of Guangdong Pearl River Talents Program (2017BT01Z032), Guangdong Provincial Key R&D Program (2019B110206002), and Natural Science Foundation of Guangdong (2019A1515010989).

Notes and references

1 D. Chen, R. Liu, Q. Lin, S. Ma, G. Li, Y. Yu, C. Zhang and T. An, *Chemosphere*, 2021, **275**, 130022.

2 C. T. Yang, G. Miao, Y. H. Pi, Q. B. Xia, J. L. Wu, Z. Li and J. Xiao, *Chem. Eng. J.*, 2019, **370**, 1128–1153.

3 C. He, J. Cheng, X. Zhang, M. Douthwaite, S. Pattisson and Z. P. Hao, *Chem. Rev.*, 2019, **119**, 4471–4568.

4 Y. M. Ji, Q. J. Shi, Y. X. Li, T. C. An, J. Zheng, J. F. Peng, Y. P. Gao, J. Y. Chen, G. Y. Li, Y. Wang, F. Zhang, A. L. Zhang, J. Y. Zhao, M. J. Molina and R. Y. Zhang, *Proc. Natl. Acad. Sci. U. S. A.*, 2020, **117**, 13294–13299.

5 M. Hakim, Y. Y. Broza, O. Barash, N. Peled, M. Phillips, A. Amann and H. Haick, *Chem. Rev.*, 2012, **112**, 5949–5966.

6 P. Wu, X. J. Jin, Y. C. Qiu and D. Q. Ye, *Environ. Sci. Technol.*, 2021, **55**, 4268–4286.

7 V. Kumar, Y. S. Lee, J. W. Shin, K. H. Kim, D. Kukkar and Y. F. Tsang, *Environ. Int.*, 2020, **135**, 105356.

8 H. L. Liu, Y. P. Ma, J. Y. Chen, M. C. Wen, G. Y. Li and T. C. An, *Appl. Catal., B*, 2019, **250**, 337–346.

9 B. Liu, J. Ji, B. Zhang, W. Huang, Y. Gan, D. Y. C. Leung and H. Huang, *J. Hazard. Mater.*, 2021, **422**, 126847.

10 W. P. Zhang, G. Y. Li, H. J. Yin, K. Zhao, H. J. Zhao and T. C. An, *Environ. Sci.: Nano*, 2021, **9**, 81–104.

This journal is © The Royal Society of Chemistry 2022

Published on 30 March 2022. Downloaded by Guangdong Technology University Library on 4/29/2022 3:10:18 AM.

11 Z. X. Zhao, S. Wang, Y. Yang, X. M. Li, J. Li and Z. Li, *Chem. Eng. J.*, 2015, **259**, 79–89.

12 X. Li, L. Zhang, Z. Yang, P. Wang, Y. Yan and J. Ran, *Sep. Purif. Technol.*, 2020, **235**, 116213.

13 X. Zhou, W. Y. Huang, J. Shi, Z. X. Zhao, Q. B. Xia, Y. W. Li, H. H. Wang and Z. Li, *J. Mater. Chem. A*, 2014, **2**, 4722–4730.

14 H. Wang, W. P. Lustig and J. Li, *Chem. Soc. Rev.*, 2018, **47**, 4729–4756.

15 U. Ryu, S. Jee, P. C. Rao, J. Shin, C. Ko, M. Yoon, K. S. Park and K. M. Choi, *Coord. Chem. Rev.*, 2021, **426**, 213544.

16 M. Woellner, S. Hausdorf, N. Klein, P. Mueller, M. W. Smith and S. Kaskel, *Adv. Mater.*, 2018, **30**, e1704679.

17 X. Cui, X. Sun, L. Liu, Q. Huang, H. Yang, C. Chen, S. Nie, Z. Zhao and Z. Zhao, *Chem. Eng. J.*, 2019, **369**, 898–907.

18 L. H. Xie, X. M. Liu, T. He and J. R. Li, *Chem.*, 2018, **4**, 1911–1927.

19 X. Li, L. Zhang, Z. Yang, P. Wang, Y. Yan and J. Ran, *Sep. Purif. Technol.*, 2020, **235**, 116213.

20 H. Li and M. R. Hill, *Acc. Chem. Res.*, 2017, **50**, 778–786.

21 W. Fan, X. Zhang, Z. Kang, X. Liu and D. Sun, *Coord. Chem. Rev.*, 2021, **443**, 213968.

22 J. Liu, J. Dong, T. Zhang and Q. Peng, *J. Controlled Release*, 2018, **286**, 64–73.

23 M. Y. Xia, Y. Xie, C. H. Yu, G. Y. Chen, Y. H. Li, T. Zhang and Q. Peng, *J. Controlled Release*, 2019, **307**, 16–31.

24 H. Sachdeva, A. Raj Khandelwal, R. Meena, K. Sharma and N. Khatik, *Mater. Today: Proc.*, 2021, **43**, 2954–2957.

25 Z. C. Xiong, Y. J. Zhu, D. D. Qin and R. L. Yang, *ACS Appl. Mater. Interfaces*, 2020, **12**, 32556–32565.

26 P. Zhang, J. Li, L. Lv, Y. Zhao and L. Qu, *ACS Nano*, 2017, **11**, 5087–5093.

27 Y. Lu, D. Fan, Y. Wang, H. Xu, C. Lu and X. Yang, *ACS Nano*, 2021, **15**, 10366–10376.

28 Y. T. Qian, F. F. Zhang and H. Pang, *Adv. Funct. Mater.*, 2021, **31**, 2104231.

29 M. Muschi, S. Devautour-Vinot, D. Aureau, N. Heymans, S. Sene, R. Emmerich, A. Ploumistos, A. Geneste, N. Steunou, G. Patriarche, G. De Weireld and C. Serre, *J. Mater. Chem. A*, 2021, **9**, 13135–13142.

30 T. Chowdhury, L. Zhang, J. Zhang and S. Aggarwal, *Mater. Adv.*, 2021, **2**, 3051–3059.

31 A. Celeste, A. Paolone, J. P. Itie, F. Borondics, B. Joseph, O. Grad, G. Blanita, C. Zlotea and F. Capitani, *J. Am. Chem. Soc.*, 2020, **142**, 15012–15019.

32 G. Ferey, C. Mellot-Draznieks, C. Serre, F. Millange, J. Dutour, S. Surble and I. Margiolaki, *Science*, 2005, **309**, 2040–2042.

33 Y. Fu, T. Mei, G. Wang, A. Guo, G. Dai, S. Wang, J. Wang, J. Li and X. Wang, *Appl. Therm. Eng.*, 2017, **114**, 961–968.

34 M. Z. Kassaee, E. Motamedi and M. Majdi, *Chem. Eng. J.*, 2011, **172**, 540–549.

35 C. Yue, L. Wu, Y. Lin, Y. Lu, C. Shang, R. Ma, X. Zhang, X. Wang, W. D. Wu, X. D. Chen and Z. Wu, *ACS Appl. Mater. Interfaces*, 2021, **13**, 26264–26277.

36 J. Ma, X. Guo, Y. Ying, D. Liu and C. Zhong, *Chem. Eng. J.*, 2017, **313**, 890–898.

37 N. Liu, W. Huang, X. Zhang, L. Tang, L. Wang, Y. Wang and M. Wu, *Appl. Catal., B*, 2018, **221**, 119–128.

38 J. He, Z. Yan, J. Wang, J. Xie, L. Jiang, Y. Shi, F. Yuan, F. Yu and Y. Sun, *Chem. Commun.*, 2013, **49**, 6761.

39 A. Modrow, D. Zargarani, R. Herges and N. Stock, *Dalton Trans.*, 2012, **41**, 8690–8696.

40 D. Chen, K. P. Taylor, Q. Hall and J. M. Kaplan, *Genetics*, 2016, **204**, 1151–1159.

41 R. Serna-Guerrero and A. Sayari, *Chem. Eng. J.*, 2010, **161**, 182–190.

42 B. Chen, I. A. Meinertzhagen and S. R. Shaw, *J. Comp. Physiol., A*, 1999, **185**, 393–404.

43 E. C. N. Lopes, F. S. C. dos Anjos, E. F. S. Vieira and A. R. Cestari, *J. Colloid Interface Sci.*, 2003, **263**, 542–547.

44 X. Wang, L. Chen and Q. Guo, *Chem. Eng. J.*, 2015, **260**, 573–581.

45 H. L. Liu, M. J. Xu, G. Y. Li, W. P. Zhang and T. C. An, *Environ. Sci.: Nano*, 2021, **8**, 543–553.

46 P. Lyu, A. M. Wright, A. Lopez-Olvera, P. G. M. Mileo, J. A. Zarate, E. Martinez-Ahumada, V. Martis, D. R. Williams, M. Dinca, I. A. Ibarra and G. Maurin, *Chem. Mater.*, 2021, **33**, 6186–6192.

47 B. Barth, M. Mendt, A. Pöppl and M. Hartmann, *Microporous Mesoporous Mater.*, 2015, **216**, 97–110.

48 Z. C. Xiong, Y. J. Zhu, D. D. Qin and R. L. Yang, *ACS Appl. Mater. Interfaces*, 2020, **12**, 32556–32565.